Assessment of Ice Shape Roughness Using a Self-Organizing Map Approach

Stephen T. McClain[1]
Baylor University, Waco, TX 76798

and

Richard E. Kreeger[2]
NASA Glenn Research Center, Cleveland, OH 44135

Self-organizing maps are neural-network techniques for representing noisy, multi-dimensional data aligned along a lower-dimensional and nonlinear manifold. For a large set of noisy data, each element of a finite set of codebook vectors is iteratively moved in the direction of the data closest to the winner codebook vector. Through successive iterations, the codebook vectors begin to align with the trends of the higher-dimensional data. Prior investigations of ice shapes have focused on using self-organizing maps to characterize mean ice forms. The Icing Research Branch has recently acquired a high resolution three-dimensional scanner system capable of resolving ice shape surface roughness. A method is presented for the evaluation of surface roughness variations using high-resolution surface scans based on a self-organizing map representation of the mean ice shape. The new method is demonstrated for 1) an 18-in. NACA 23012 airfoil at 2° AOA just after the initial ice coverage of the leading 5% of the suction surface of the airfoil, 2) a 21-in. NACA 0012 at 0° AOA following coverage of the leading 10% of the airfoil surface, and 3) a cold-soaked 21-in. NACA 0012 airfoil without ice. The SOM method resulted in descriptions of the statistical coverage limits and a quantitative representation of early stages of ice roughness formation on the airfoils. Limitations of the SOM method are explored, and the uncertainty limits of the method are investigated using the non-iced NACA 0012 airfoil measurements.

Nomenclature

AOA	=	angle of attack
b	=	codebook vectors
$h(i,j)$	=	neighborhood function of i to j codebook vectors
j	=	codebook vector index
LWC	=	liquid water content
M	=	number of codebook vectors
MVD	=	median volumetric diameter
N	=	airfoil or mean ice shape surface normal coordinate direction
R^d	=	high-dimensional data space
RMH	=	roughness maximum height
R_q	=	the root-mean-square roughness height
SOM	=	Self-Organizing Map
S	=	airfoil or mean ice shape surface tangential coordinate direction
x	=	element of data set
α	=	local direction angle of manifold through a codebook vector
β	=	manifold
γ	=	direction angle of surface point relative to manifold direction through winning codebook vector

---

[1] Assistant Professor, Mechanical Engineering Department, One Bear Place #97356, and Senior Member AIAA.
[2] Aerospace Engineer, Icing Research Branch, 21000 Brookpark Rd., Senior Member AIAA.

δ =   scaling parameter governing neighborhood size

η =   learning rate

I. Introduction

THE deleterious effects of ice roughness on aircraft performance and safety have been recognized since the early investigations into the ice accretion process. Ice roughness increases the skin friction drag, increases the rate of heat transfer from the freezing water layer to the airstream, and induces higher levels of turbulence in the airflow than would be observed on mean representative ice shapes without roughness. Further, ice roughness increases the droplet capture efficiency of the local surface relative to a smooth surface.

While ice roughness and its geometric properties have been recognized as critical to the ice accretion process and to the reduction in iced aircraft performance in icing conditions, describing the nature of ice accretion roughness is not trivial. Classical studies of ice roughness during short-duration icing events include Anderson and Shin [1], Anderson et al. [2], and Shin [3]. For the measurements of Anderson and Shin [1], Anderson et al. [2], and Shin [3], images were acquired of the ice surface from multiple directions. Image analysis techniques were then used to determine the dimensions of each roughness element and the spacing to its nearest neighboring roughness element. The methods used in the classical studies were extremely laborious in terms of manual identification of each roughness element, use of the image analysis equipment, and identification of the roughness element in multiple images.

Recent improvements in laser scanning approaches have the potential to revolutionize the process of ice accretion shape characterization and surface roughness evaluation [4]. However, laser scans of ice shapes or castings of ice shapes present challenges. First, the scans typically result in point densities of 5000 points per cm^2 of scanned surface area. For the leading edges of two-dimensional wings (airfoils) used in the NASA icing tunnel, which have 18 to 21 in. chord lengths, ice shape scans with a 10-cm spanwise width typically result in more than 1 million measurement points. Secondly, on two-dimensional airfoils, horn structures and the geometrically closed-loop nature of airfoils lead to multi-valued functions describing the airfoil surface. The multi-valued function description of airfoils with complex horn shapes results in situations where standard regression cannot be employed to describe the entire airfoil at once. To evaluate the roughness along an iced airfoil, the mean ice-shape or ice form must be extracted. Thirdly, the radii of curvature of horn structures may be on the same order of magnitude as the roughness heights for long-accretion time ice shapes. The comparable sizes of horn structures and roughness creates difficulties in discerning the difference between ice form changes and roughness features. Finally, most ice shapes, even on straight wings, have considerable three-dimensional variations along the span of the wing.

Clustering methods for non-linear manifold detection have the potential for enabling a more rigorous evaluation of ice shape roughness. One example of a clustering method for manifold detection is a neural network concept called a self-organizing map (SOM) [5]. The SOM approach uses an iteratively-placed set of codebook vectors to represent "clumps" of data relative to a spline-surface through a set of control points. McClain et al. [6] applied the SOM approach to characterize the nature of airfoils with Rime ice, glaze ice, and multi-horn ice shapes. The primary objective of McClain et al. [6] was to demonstrate how the SOM could be used not only to capture the mean ice form or shape, but to expand the SOM approach using multi-dimensional statistics to characterize the ice-surface coverage limits. Interpreting the coverage limits of the SOM ice shape descriptions as experimental uncertainties, the method of McClain et al. [6] enables a more rigorous comparison of measured ice shapes to ice shape predictions from codes such as LEWICE [7] or FENSAP-ICE [8].

In this study, the SOM and multi-dimensional statistics approach of McClain et al. [6] are extended to evaluate the of the roughness variations along the surface of two-dimensional airfoils. By treating the daisy-chain of SOM control points as a representation of the continuous mean ice surface, the daisy-chain may be unwrapped using simple geometry. The two-dimensional scatter of the clump of data around each manifold control point is then used to describe the local roughness along the manifold near the control point.

To explore the limits of the approach and the new laser scanning equipment described by Lee et al. [4] for evaluation of ice roughness variations, the approach was applied to three airfoils tested in the Icing Research Tunnel at the NASA Glenn Research Center. The airfoils measured were 1) an 18-in. NACA 23012 with 2° AOA exposed to a 15-μm MVD, 0.75 gm/m³ cloud for 30 s in a 102.9 m/s, -2.2 °C flow, 2) a NACA 0012 with 0° AOA exposed to a 30-μm MVD, 0.6 gm/m³ cloud for 94 s in a 67 m/s, -4.7 °C flow, and 3) a 21-in. NACA 0012 airfoil that had been cold-soaked to -4.7 °C in 67 m/s flow without ice accretion. Each airfoil test model or wing used in this study is straight (no sweep). Thus, the mean or representative ice shapes are assumed to be inherently two-dimensional.

II. Self-Organizing Maps

The Self-Organizing Map, or sometimes referred to as a Kohonen Map, is a clustering method for the detection of non-linear manifolds in multi-dimensional space [5]. Figure 1 shows three-dimensional data scattered about a one-dimensional manifold, β, which is inherently one-dimensional. In a signal-processing application, the data in Figure 1 is noisy and requires significant memory. If information about β could be obtained, the "trend" of the noisy data could be transmitted much less expensively than transmitting the complete noisy data set. In most signal processing applications, the important question is "how can the nature of β be determined using the experimental data?"
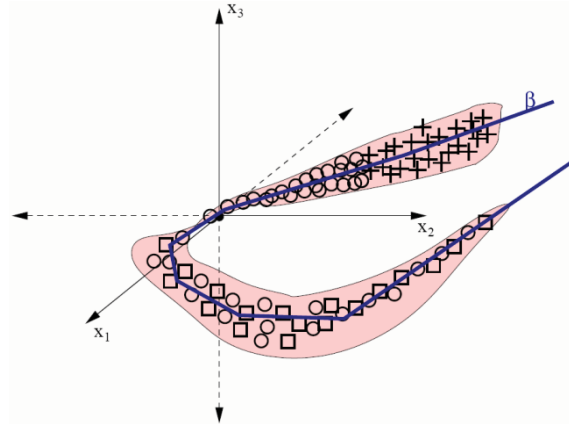

Figure 1. Point Cloud Scattered about a One-Dimensional Manifold [9]

SOMs depend on the use of codebook vectors, **b**, to represent clumps of data, depicted in Fig. 2. When a series of codebook vectors are connected, the one-dimensional manifold guiding the data in Fig. 2 is represented by the spline through the codebook vectors. To develop the codebook vectors, an initial shape or random distribution of the vectors is determined. The codebook vectors are then moved in the direction of the clump of points to which the codebook vector is closest. Like most neural network approaches, the SOM requires a learning or training process. Over iterative moves, the codebook vectors spread out and settle into their local clumps.
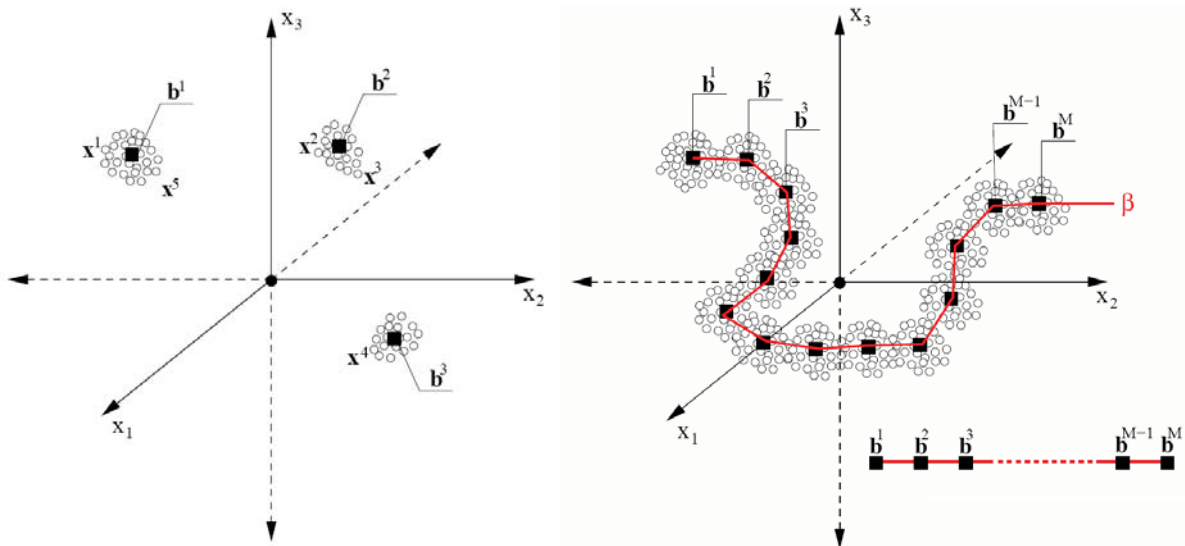

Figure 2. Self-Organizing Map Representation of Point Cloud [9]

The self-organizing map can be best described as a constrained clustering method [9]. Consider a data set of high dimensional points aligned (up to some noise) along a lower dimensional manifold embedded in the high-

American Institute of Aeronautics and Astronautics

dimensional data space, R^d, as depicted in Figure 1. In SOM, such a data set is described through a collection of M codebook vectors $b^j \in R^d$, j = 1,2,...,M, living in the data space. Each codebook vector, b^j, represents the region of the data space around it (Voronoi compartment of b^j), such that all data points in that region are closer to b^j than to any other codebook vector. Crucially, a topological neighborhood structure is imposed on the codebook using a neighborhood function $h(i,j)$, i,j=1,2,...M. Higher values of $h(i,j)$ signify that codebook vectors b^i, b^j should be neighbors (e.g. lie close to each other in the data space). Smaller values of $h(i,j)$ mean that no such requirement applies.

During the training process, the codebook vectors get adapted to the data set so that the quantization error (resulting from representing each original data point x by the codebook vector $b^{win(x)}$ closest to it) is minimized and, at the same time, the layout of codebook vectors b^j in the data space respects the neighborhood properties dictated by the neighborhood function $h(i,j)$. For a one-dimensional data structure, e.g. Figure 1, one simply prescribes that the representative codebook vectors b^j must lie on a "bicycle chain" embedded in the data space. This corresponds to imposing a linear order on the codebook vector indexes 1<2<3<...<M and defining

$$h(i,j) = exp(-\frac{(i-j)^2}{\delta^2}), \ i,j = 1,2,...,M,$$

where δ is the scale parameter governing the neighborhood size.

During the training phase, data points are iteratively selected from the data set and for each data point x, all codebook vectors are moved from their current positions closer to x. By how much each codebook vector b^j gets moved depends on how close we want b^j to be to the principal representative $b^{win(x)}$ of x. The closer b^j should be to $b^{win(x)}$, as measured by the value $h(win(x),j)$ of the neighborhood function, the more it gets moved towards x. The update equation can be summarized as

$$b^j \leftarrow b^j + h(win(x),j) \cdot \eta \cdot (x - b^j), \ j = 1,2,...,M,$$

where η is a positive real number, called the learning rate, modulating the proportions of codebook vector updates.

To ensure convergence of the algorithm, the learning rate, η, is made to decrease over time (e.g. exponentially) from some initial value to 0. It can be shown that in order to preserve the neighborhood relations among the codebook vectors, it is recommended that the neighborhood scale parameter, δ, decreases over time as well. Starting with a broader neighborhood (higher value of δ) enabling rough ordering of codebook vectors in the data space, the neighborhood size is gradually decreased, leading to a more selective codebook ordering.

The SOM approach is one of several different dimensionality reduction or manifold learning strategies that could be used for ice shape characterization. For example, Laplacian Eigenmaps [10] or Generative Topographic Mapping [11] could also be used for ice shape and ice roughness characterization in a similar manner. The important aspect of the manifold learning strategy for ice characterization is that local neighborhoods of the point cloud are associated with each codebook vector as part of the learning process. These associated regions or neighborhoods of the point cloud lend themselves to the evaluation of local neighborhood statistics. This process allows the manifold to be characterized, representing the mean ice shape, and the distribution of the experimental surface measurements about the manifold, that is, the measurement noise caused by the roughness of the ice shape, to be characterized as well.

Application to Ice Shape Characterization

The nature of the SOM method and the positioning of the codebook vectors along a "daisy-chain" enable a more rigorous validation method for ice accretion codes when combined with multi-dimensional statistical descriptions. Since the "clumps" of points are distributed about the codebook vectors, the deviations of the point measurements in the clumps can be used to evaluate the coverage statistics and uncertainty of the codebook vector representation. Figure 3 demonstrates how each surface measurement is used to determine a deviation from the spline surface through the control points or codebook vectors.

Figure 3 shows a single surface measurement $\mathbf{x}^j$, its winning codebook vector $\mathbf{b^n}$, and the two neighboring codebook vectors along the daisy-chain of codebook vectors representing the manifold. In the approach used for this study, the manifold is assumed to be a first-order manifold in two-dimensional space with the characteristic that at each codebook vector, the local slope of the manifold is equal to the central finite-difference evaluated using the two closest surrounding codebook vectors. The approach used assumes that all deviations from the manifold are normal to the manifold. That is, the deviation of a surface measurement normal to the line through the codebook

American Institute of Aeronautics and Astronautics

vector with the local slope set by the neighboring codebook vectors is considered the "height" of the surface point above or below the local manifold.

To calculate the local height, of any point, $\mathbf{x}^j$, relative to the manifold, the two neighboring codebook vectors are first used to calculate the direction of the manifold through $\mathbf{b^n}$ using

$$\alpha_{\mathbf{b^n}} = arctan\left[\frac{y_{\mathbf{b^{n+1}}} - y_{\mathbf{b^{n-1}}}}{x_{\mathbf{b^{n+1}}} - x_{\mathbf{b^{n-1}}}}\right] \tag{1}$$

The direction of the $\mathbf{x}^j$ point from its winning codebook vector relative to the line through the codebook vector with the direction α is then found using

$$\gamma_{\mathbf{x}^j} = arctan\left[\frac{y_{\mathbf{x}^j} - y_{\mathbf{b^n}}}{x_{\mathbf{x}^j} - x_{\mathbf{b^n}}}\right] - \alpha_{\mathbf{b^n}} \tag{2}$$

The normal height the $\mathbf{x}^j$ point from the line through its winning codebook vector is then determined using

$$dN_{\mathbf{x}^j} = \left[\left(x_{\mathbf{x}^j} - x_{\mathbf{b^n}}\right)^2 + \left(y_{\mathbf{x}^j} - y_{\mathbf{b^n}}\right)^2\right]^{\frac{1}{2}} sin\left(\gamma_{\mathbf{x}^j}\right) \tag{3}$$
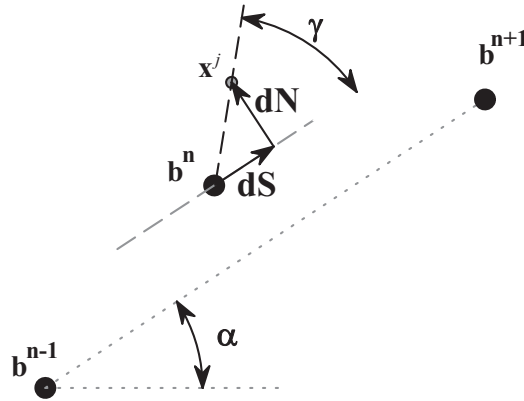

Figure 3. Metrics of Local Point about a Codebook Vector

The normal height of all the points related to an individual codebook vector may then be used to calculate statistics such as those commonly used to calculate traditional roughness parameters. For example, the root-mean-square roughness height for a rough surface is traditionally described as

$$R_q = \left[\frac{1}{J}\sum_{j=1}^{J}\left(y_j - \bar{y}\right)^2\right]^{\frac{1}{2}} \tag{4}$$

Based on the SOM-manifold description used here, the root-mean-square roughness height is calculated at each codebook vector as

$$R_q = \left[\frac{1}{J}\sum_{j=1}^{J}N_{\mathbf{x}^j}^2\right]^{\frac{1}{2}} \tag{5}$$

In traditional roughness studies, the 99% roughness maximum height (RMH) based on a Gaussian distribution is calculated using three times the root-mean roughness height.

$$RMH_{\mathbf{b^n}} = 3R_q == 3\left[\frac{1}{J}\sum_{j=1}^{J}N_{\mathbf{x}^j}{}^2\right]^{\frac{1}{2}} \tag{6}$$

Where J is the number of surface points for which $\mathbf{b^n}$ is the winning (closest) codebook vector.

In McClain et al. [6], the objective was to use the deviations from the manifold to generate inclusion or uncertainty limits as opposed to creating roughness descriptions. The generation of the ice shape inclusion limits was intended to improve the ice accretion code validation process. Figure 4 presents the 95% Gaussian inclusion limits for a horn ice-shape evaluated using the methods of McClain et al. [6]. From a validation perspective, if the predicted ice shape from LEWICE or FENSAP-ICE were to fall inside the inclusion limits of a measured ice shape, then the ice accretion simulation would be considered validated.
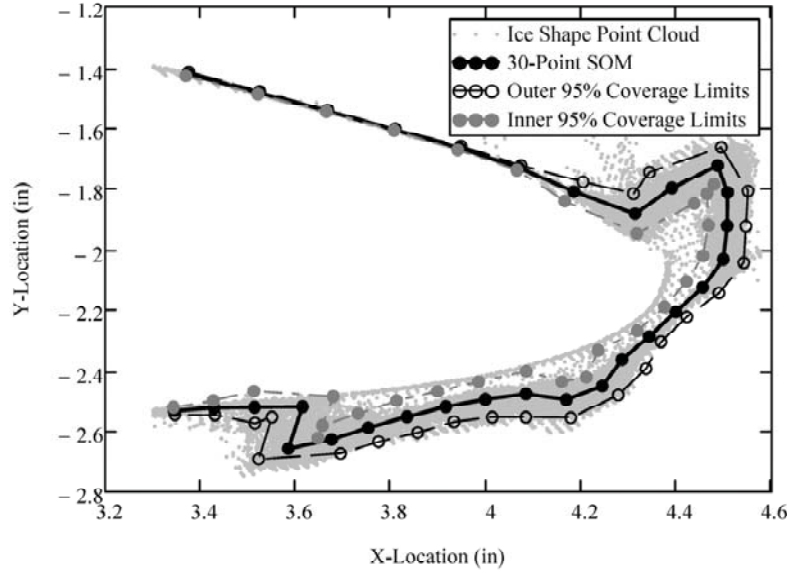

Figure 4. Coverage Limits of a Horned Ice Shape Evaluated Using Local Point Statistics

Surface Unwrapping

An important aspect of the roughness evaluation is the unwrapping of the surface in the airfoil surface coordinates. To predict the effects of the roughness using traditional boundary layer approaches, the surface must be described in terms of the traditional airfoil surface coordinates. To evaluate the distance along the manifold representing the mean ice shape, a discrete arc-length approach is taken. That is, at one end of the daisy chain, the length of the arc is set to zero or a known value from the stagnation point on the airfoil. The position of the next codebook vector is then evaluated as the straight-line distance between the two codebook vectors as demonstrated in Eq. (7).

$$S_{\mathbf{b^n}} = S_{\mathbf{b^{n-1}}} + \left[\left(x_{\mathbf{b^n}} - x_{\mathbf{b^{n-1}}}\right)^2 + \left(y_{\mathbf{b^n}} - y_{\mathbf{b^{n-1}}}\right)^2\right]^{\frac{1}{2}} \tag{7}$$

Once the surface distance coordinate of each codebook vector is determined, the surface distance coordinate of each point cloud measurement may be evaluated based on the location of the surface point's winning codebook vector. Revisiting Figure 3, once the angle of the $\mathbf{x}^j$ point with respect to the surface manifold through its winning codebook vector (γ) is known, the surface projection along the manifold is found using

$$S_{\mathbf{x}^j} = S_{\mathbf{b^n}} + dS_{x^j} = S_{\mathbf{b^n}} + \left[\left(x_{\mathbf{x}^j} - x_{\mathbf{b^n}}\right)^2 + \left(y_{\mathbf{x}^j} - y_{\mathbf{b^n}}\right)^2\right]^{\frac{1}{2}} cos\left(\gamma_{\mathbf{x}^j}\right) \tag{8}$$

The straight-line arc length approach of Eq. (7) is not the only option for evaluating the length of the manifold between the codebook vectors. An approach that connects the codebook vectors using the lines through

American Institute of Aeronautics and Astronautics

the codebook vectors with the directions and slopes evaluated using Eq. (1) may be a more appropriate method than that presented in Eq. (7). However, the salient features of any unwrapping process are captured by the method employing Eqns. (7) and (8). Those critical features being 1) the distance between the codebook vectors along the manifold are calculated and then 2) the projected distance of each surface point from its winning codebook vector is calculated relative to the directions tangent to and normal to the manifold passing through the winning codebook vector.

III. Ice Roughness Analysis Using Self Organizing Maps

The methods presented for ice roughness and surface unwrapping were applied to two airfoils with short-duration ice accretion surfaces and one cold-soaked airfoil without roughness. The two iced airfoils and conditions were chosen for the initial investigation because their dominant ice accretion features are roughness. Since the surfaces chosen were from short-duration icing events, the form or shape changes to the aircraft properties were not as significant as the roughness or surface condition changes. The non-iced airfoil was measured to validate the SOM roughness evaluation process and to assess the uncertainty limits or resolution of the approach. Table 1 presents a summary of the icing event parameters used for the two iced airfoil measurements.

Table 1. Summary of Icing Event Parameters for Airfoils Studied

Airfoil	Chord (cm)	AOA	Air Speed (m/s)	Temp (°C)	LWC (gm/m^3)	MVD (μm)	Event Duration (s)
NACA 23012	45.7	2°	102.9	-2.2	0.75	15	30
NACA 0012	53.3	0°	67	-4.7	0.6	30	94
NACA 0012	53.3	0°	67	-4.7	n/a	n/a	n/a

Airfoil Surface Roughness Measurements

The ice accretion tests and cold-soak test were performed in the NASA Glenn Icing Research Tunnel. Following the wind tunnel tests, a Romer Absolute Arm system was used to generate surface point-clouds for each of the surfaces studied. The point clouds were created using scans of approximately a 10-cm spanwise strip of the leading 10-cm of the airfoil. The complete point clouds for each test contained approximately one million surface measurements. The complete point cloud for the NACA 23012 is presented in Figure 5. Because of limitations with the SOM analysis software used, each point cloud was reduced to approximately 100,000 points. The point cloud reduction was performed using the spanwise center sections of each point cloud. Figure 6 presents the reduced point cloud for the NACA 23012 airfoil, which is a 2.54 cm (1 in.) spanwise section.
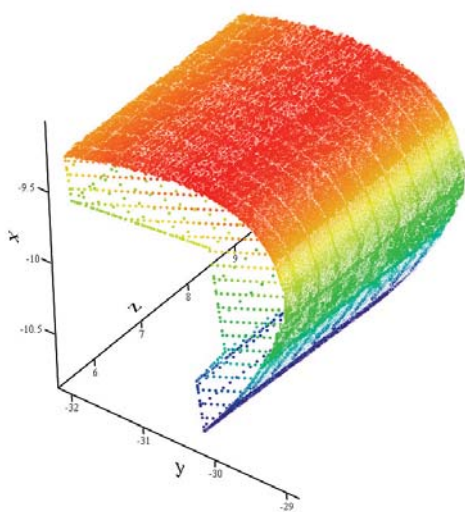

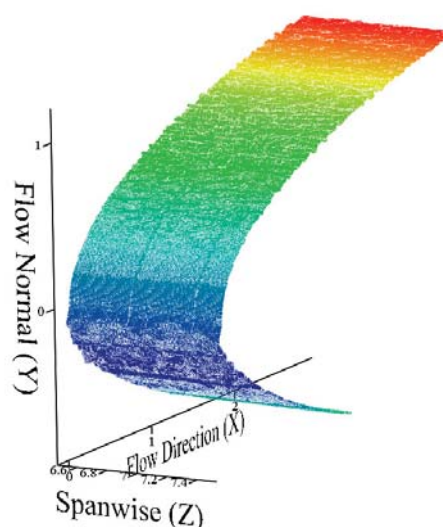*Figure 5. Ice Shape Point Cloud with Roughness (dimensions shown in inches)*

Figure 6. One-Inch Strip from Spanwise Center of Point Cloud

American Institute of Aeronautics and Astronautics

Figure 7 presents the two-dimensional or X-Y projection of the three surfaces measured for this study. Figure 7 provides a qualitative view of the limitations associated with quantifying a 3D roughness field using a two-dimensional approach. Figure 7 also demonstrates that the ice accretion process resulted primarily in surface roughness. Figure 7(a), which shows the projection of the NACA 23012, exhibits the most significant shape changes, which occurs near the leading edge on the suction surface of the airfoil. In Figure 7(c), it should be noted that the apparent angle of attack demonstrated in the projected point cloud is a rotation of the airfoil relative to the Romer Absolute's coordinate system and not an angle of attack relative to the wind tunnel flow.
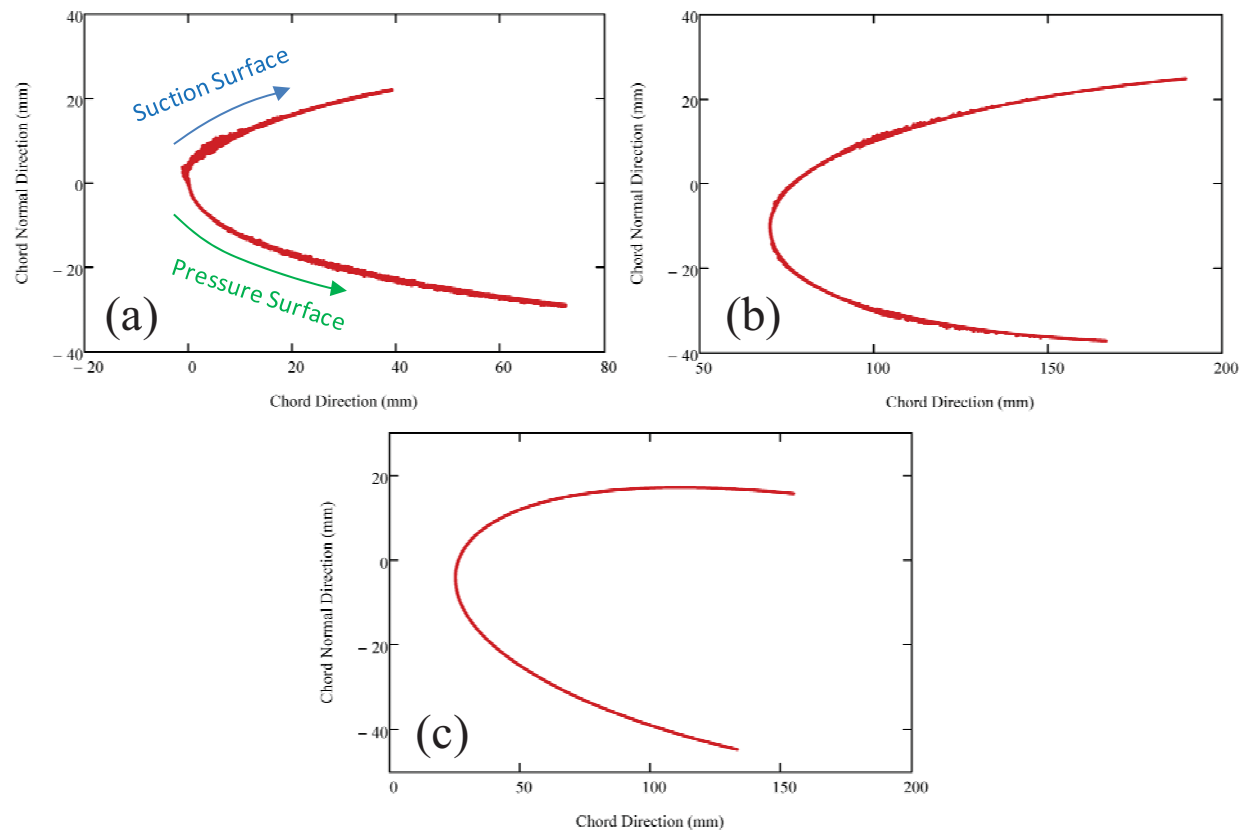

Figure 7. X-Y Projections of Surface Point Clouds: (a) NACA 23012, (b) NACA 0012 with Ice Roughness, (c) Cold-Soaked NACA 0012 without Ice

Application of SOM to Ice Shape Point Cloud

The three point clouds were analyzed using the JAVA applet BSOM1 [12]. Initially, BSOM1 places a random distribution of codebook vectors in the ice shape domain. Running BSOM1 with a random initial placing of the codebook vectors produces a final ice shape characterization where the codebook vectors adequately capture the ice shape, but the points are out of order along the arc-length of the manifold (nonbicycle-chained). To create ice shape characterizations with ordered points along the arc-length of the ice shape, the initial points were manually placed in order along a shape that resembled the first 15% the airfoil. BSOM1 was then set to "automatic learning" and run until significant movement of the codebook vectors could not be detected. The resulting codebook vectors from BSOM1 and the point clouds were then read into Mathcad to generate the coverage limits, to perform the roughness evaluation, and to unwrap the surface into the airfoil surface coordinates.

The SOM representations and coverage limits of the airfoil surface measurements are presented in Figure 8. Figures 8(a), 8(b), and 8(d) present SOM representations with codebook vectors placed nominally 6 mm apart along the one-dimensional manifolds for the NACA 23012, the iced NACA 0012, and the non-iced NACA 0012, respectively.

As noted by McClain et al. [6], the self-organizing maps have difficulty in representing manifolds with low noise and very low radii of curvature such as those found on Rime ice shapes at the very leading edges of non-iced

8
American Institute of Aeronautics and Astronautics

airfoils. Figures 8(c) and 8(e) present SOM representations of the iced NACA 0012 and the non-iced NACA 0012, respectively, where the SOM representations of the leading edge of the airfoil point clouds were refined to codebook vector spacings of 1-mm along the manifold. To create the refined SOM representations, the leading edge section (representing approximately 50 mm of the manifold length) were extracted. BSOM1 was then run on the extracted leading-edge point clouds. The codebook vectors representing the extracted sections in the original 40-point SOM representations were then replaced with the new SOM representations of the leading-edge section.
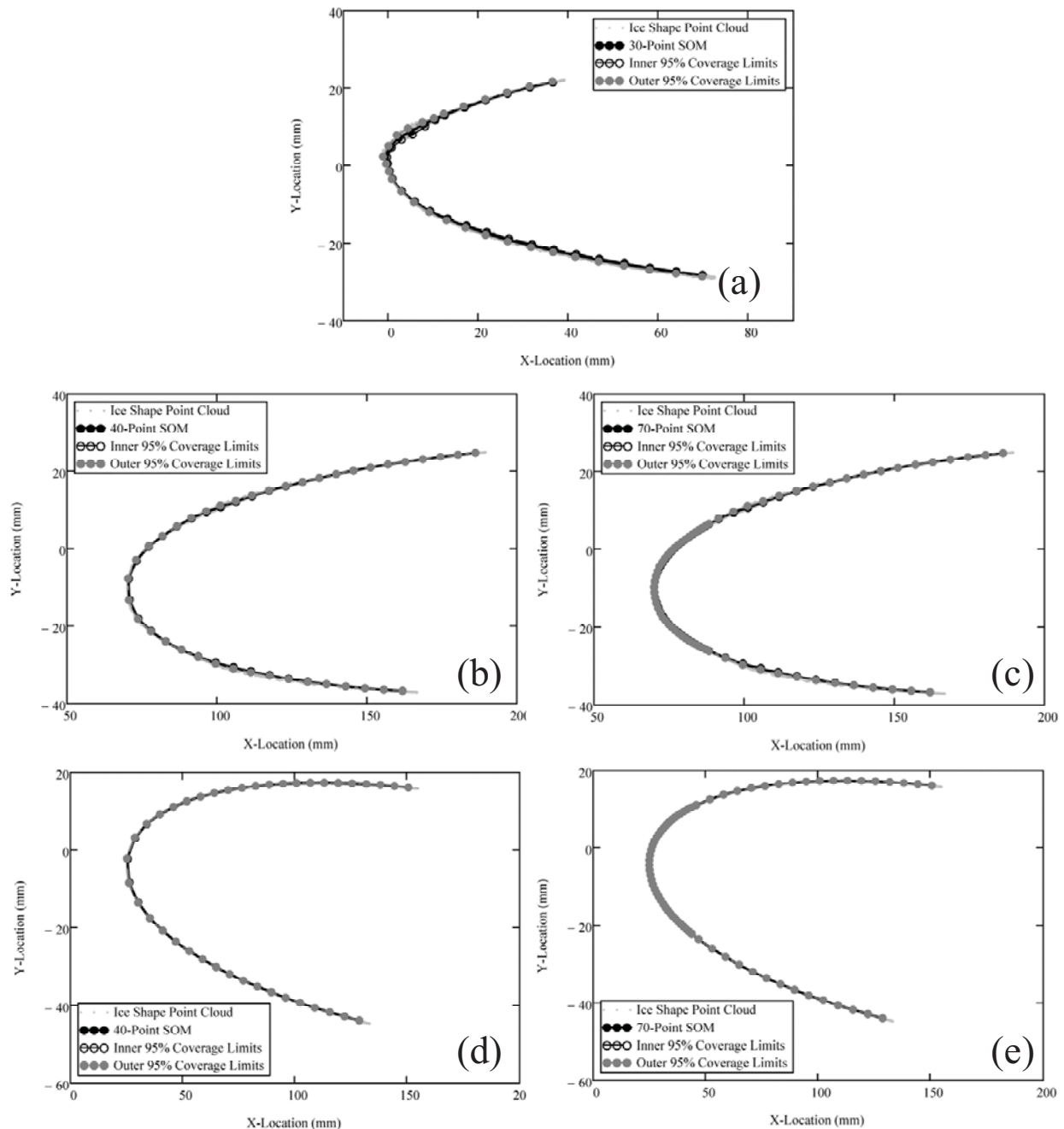
Figure 8. SOM Representations and Coverage Limits of the Three Airfoils Investigated: (a) 30-Point SOM Representation of NACA 23012 airfoil, (b) 40-Point SOM Representation of NACA 0012 with Ice Roughness, (c) Refined 70-Point SOM Representation of NACA 0012 with Ice Roughness, (d) 40-Point SOM Representation of NACA 0012 without Ice Roughness, and (e) Refined 70-Point SOM Representation of NACA 0012 without Ice Roughness

American Institute of Aeronautics and Astronautics

Evaluation of Unwrapped Roughness

While the unwrapped roughness characteristics are critical for the prediction of skin friction and convection coefficients using traditional boundary-layer approaches, the unwrapping process also allows for a clearer visualization of the roughness variations along an iced airfoil. For example, Figure 9 presents the unwrapped projection of the NACA 23012 point cloud on the S-N plane, where S is the direction that is tangent to the mean manifold surface at each location, and N is the direction normal to the mean surface at each location. The value of S at each surface location represents the arc-length along the mean airfoil surface. In Figure 9, positive values of the mean shape surface distance (S), are along the suction surface of the airfoil caused by the angle of attack of the NACA 23012, and negative values of mean shape surface distance are along the pressure side of the airfoil.
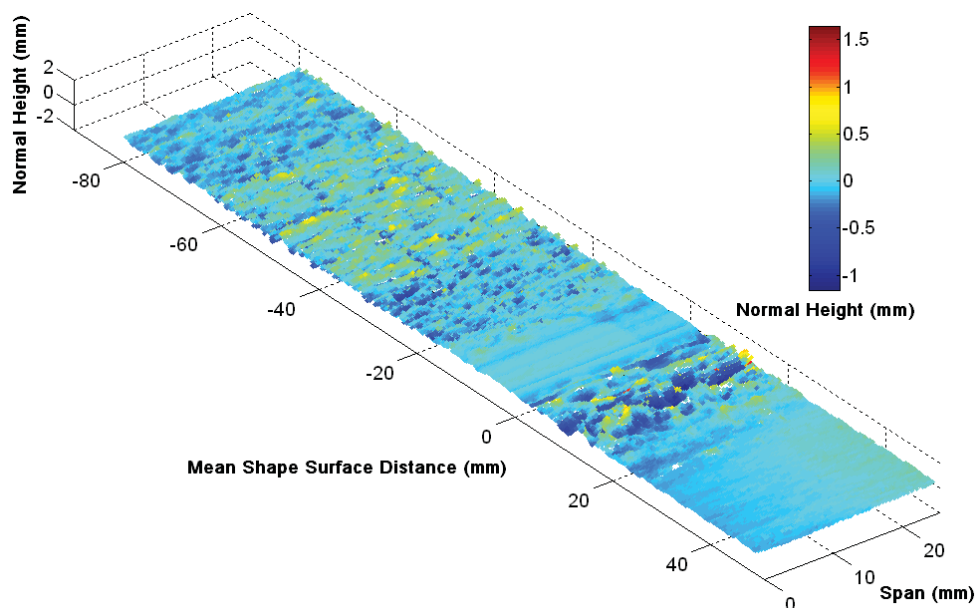

Figure 9. Unwrapped Representation of the NACA 23012 Surface

Figure 10 presents the unwrapped point clouds of the three surfaces projected on the S-N plane. Figures 10(a), 10(b), and 10(d) present the initial S-N point cloud projections for the NACA 23012, the iced NACA 0012, and the non-iced NACA 0012, respectively. Figures 10(c) and 10(e) present S-N projections of the iced NACA 0012 and the non-iced NACA 0012, respectively, based on the refined 70-point SOM representations.

In Figures 10(b)-10(e), which were generated for a symmetric airfoil at 0° AOA, the datum or "zero point" for the mean shape surface distance is set at the stagnation points of the airfoils. Figures 10(b) and 10(d) indicate the need for the refinement of the initial 40-point SOM representations of the airfoils. Near the stagnation point where the radii curvature of the airfoil shapes are the smallest, the sparseness of the initial SOM representations creates artificial arcs in the unwrapped point clouds that cause errors in the calculations of the local roughness characteristics. In the SOM learning process, each codebook vector is moved towards the center of the "cluster" of points for which the vector is the winning codebook vector. As such, when the SOM representation is too sparse, i.e. greater than the local radius of curvature of the manifold, then the codebook vector is placed at the centroid of the cluster and does not follow the manifold through the point cluster. Figures 10(c) and 10(e) demonstrate that arcs are not apparent in the refined SOM representations.

Figure 11 presents the roughness maximum heights, described by Eq. (6), evaluated at each codebook vector location along the unwrapped manifold mean surface distance. Figure 11(a) shows the distinct difference between the roughness properties on the suction side of the airfoil to the pressure side of the airfoil at 2° AOA. The roughness differences are caused by the differences in collection efficiency and the differences in kinetic cooling of the airstream as it increases velocity around the airfoil surfaces.

Figure 11(b) and Figure 11(d) further demonstrate the necessity for the refinement of the initial 40-point SOM representations. In Figs. 11(b) and 11(d), the artificial arcs created by the sparse SOM representations cause the RMH values to be overestimated near the leading edge. Revisiting Figure 7(b), the iced NACA 0012 has two regions of significant roughness on both the top and bottom sides of the airfoil. In Figure 11(b), the roughness

American Institute of Aeronautics and Astronautics

regions on the top and bottom of the airfoil near the leading edge are essentially lumped together. The smooth stagnation region between the two leading edge roughness regions is not apparent in the sparse SOM representation. In Figure 11(d), the sparse SOM representation creates an artificial 0.6-mm RMH at the leading edge of the non-iced NACA 0012 airfoil.
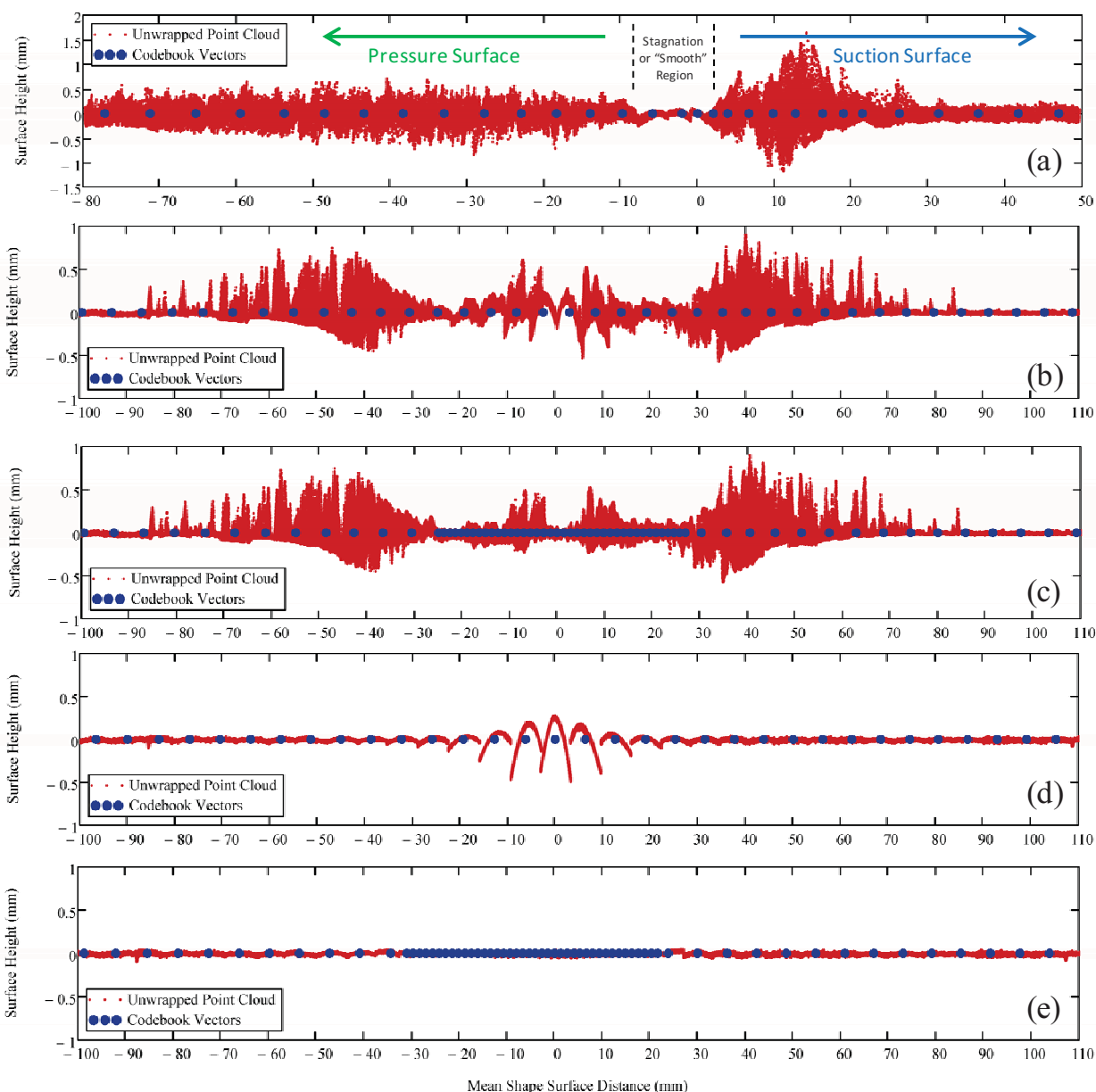
Figure 10. S-N Projections of the SOM Representations and the Surface Point Clouds: (a) 30-Point SOM Representation of NACA 23012 airfoil, (b) 40-Point SOM Representation of NACA 0012 with Ice Roughness, (c) Refined 70-Point SOM Representation of NACA 0012 with Ice Roughness, (d) 40-Point SOM Representation of NACA 0012 without Ice Roughness, and (e) Refined 70-Point SOM Representation of NACA 0012 without Ice Roughness

After refinement, the 70-point SOM representations capture the roughness variations along the iced and non-iced NACA 0012. Figure 11(c) shows four distinct roughness regions with a smooth zone at the stagnation point of the airfoil. Figure 11(c) also demonstrates that the ice roughness properties are nearly, but not exactly, symmetrical. The iced NACA 0012 exhibits two roughness zones at about +9 and -9 mm from the stagnation point. Two other, larger roughness zones are centered about +41 and -41 mm from the stagnation point.

Finally, Figure 11(e) shows that with the refined SOM representation, the largest RMH reported for the non-iced NACA 0012 is 83.1 μm, which occurs at the transition edge between the initial SOM representation and the refined SOM representation. In the refined region near the stagnation point, the average RHM is 29.5 μm. The average value of RHM near the stagnation point of the non-iced NACA 0012 is near the resolution limits of the Romer Absolute Arm system. Based on the level of RMH values for the non-iced NACA 0012, the case serves as an excellent validation of the Romer Absolute Arm system and the roughness evaluation approach.
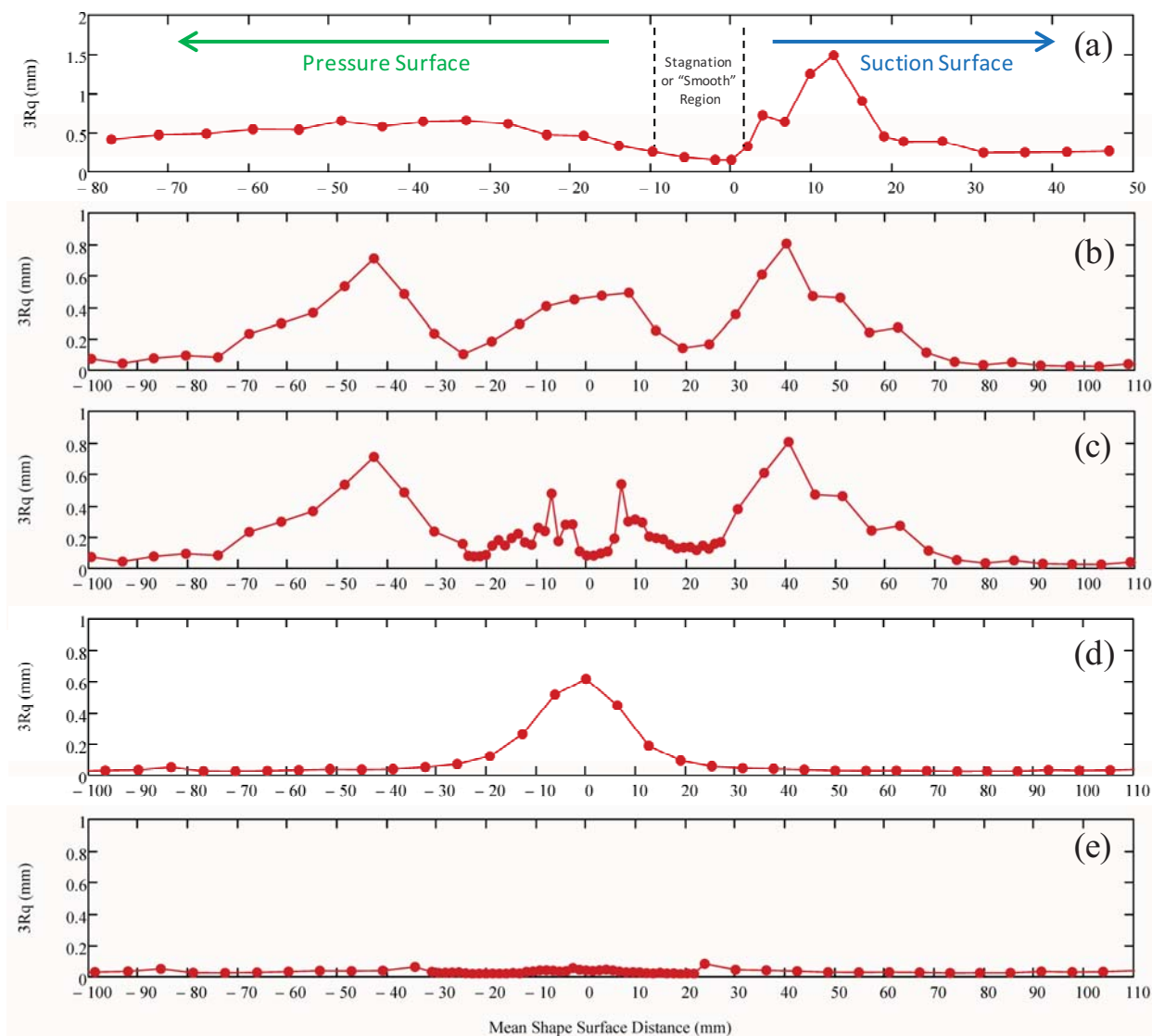
Figure 11. S-N Projections of the Variations in Surface Roughness along the Airfoil Surfaces: (a) 30-Point SOM Representation of NACA 23012 airfoil, (b) 40-Point SOM Representation of NACA 0012 with Ice Roughness, (c) Refined 70-Point SOM Representation of NACA 0012 with Ice Roughness, (d) 40-Point SOM Representation of NACA 0012 without Ice Roughness, and (e) Refined 70-Point SOM Representation of NACA 0012 without Ice Roughness

While the SOM roughness approach captures the important variations in roughness of the two iced airfoils, several areas for improvement and future work are apparent. First, while the consecutive application of the SOM approach for surface refinement in the leading edge region was successful in capturing the multiple roughness regions on the iced NACA 0012 and in approaching the scanner resolution limits for the non-iced NACA 0012, the consecutive approach is somewhat *ad hoc*. As apparent in Figure 11(e), at the transition between the initial and the refined zones, the roughness is overestimated because the initial codebook vectors are not allowed to readjust to

their subsequent cluster of points. An approach called the Growing Self-Organizing Map may enable automatically refined SOM representations of ice shapes in future studies [13].

The second area for future investigation is a validation of the new scanning measurements with surface roughness characterized using roughness measurement approaches similar to that used in the historical ice roughness experiments by Anderson and Shin [1], Anderson et al. [2], and Shin [3]. In the historical roughness investigations, the dimensions of individual ice roughness elements were measured using image analysis. To validate the laser scanning approach and provide a deeper understanding into comparisons of discrete roughness element measurements to statistical roughness representations such as the 99% Gaussian Roughness Maximum Height (RMH), methods must be developed to convert the laser scan measurements into roughness metrics similar to those acquired in the historical roughness studies.

Thirdly, the approach or improved SOM approach will be used to extend the historical ice roughness studies and include roughness changes over time and for various Appendix C and SLD icing conditions. The historical measurements of Anderson and Shin [1], Anderson et al. [2], and Shin [3] were confined to Appendix C icing conditions [14]. High resolution surface scans have been recently performed to replicate some of the Anderson et al. [2] cases and extend the roughness characterizations in SLD conditions.

Finally, all of the applications of the SOM to this point have been for airfoils or wings with negligible variations in the spanwise direction. While straight wings are an important part of modern aviation, many air vehicles have wings and surfaces with spanwise variations. Just as with two-dimensional wings (airfoils), the ice roughness that forms on a swept wing during the initial stages of an icing event are critical to the resulting ice shape that is formed in later stages of the icing event. In future investigations, an SOM or alternative non-linear manifold detection scheme must be employed to evaluate the roughness variations on swept wings and other three-dimensional aircraft structures.

IV. Conclusions

Advanced methods are required to process the high fidelity measurement techniques being used to characterize wind tunnel ice shapes and ice roughness. The SOM technique approach of McClain et al. [6] was extended to evaluate the roughness of three test airfoil surfaces. An unwrapping process was developed to visualize the roughness variations and express the roughness variations in terms of traditional airfoil surface coordinates. The analysis resulted in a generation of statistical coverage limits and a quantitative representation of the very earliest stages of ice roughness formation on an airfoil.

The limitation of the SOM method in capturing regions of the manifold with small radii of curvature and relatively low roughness was a primary observation of the study. A refinement of the SOM characterizations near the leading edges of the airfoils allowed characterizations of the iced and non-iced NACA 0012 airfoils that reflected qualitative observations of the point clouds. The refined SOM characterization of the non-iced NACA 0012 resulted in roughness characteristics that approached the spatial resolution of the laser scanning system used for the study.

Future work to improve the method will 1) investigate automatic SOM refining methods and 2) validate historical roughness measurements using the high resolution laser scanning approaches. In the near future, the SOM approach presented here or alternative non-linear manifold detection schemes will be employed to expand SLD roughness studies on straight and swept wings.

V. Acknowledgments

VI. References

[1]Anderson, D. N., and Shin, J., (1997), "Characterization of Ice Roughness from Simulated Icing Encounters," NASA TM-107400.

[2]Anderson, D. N., Hentschel, D. B., and Ruff, G. A., (1998), "Measurement and Correlation of Ice Accretion Roughness," NASA CR—2003-211823.

[3]Shin, J., (1994), "Characteristics of Surface Roughness Associated With Leading Edge Ice Accretion," NASA TM-106459.

[4]Lee, S., Broeren, A., Addy, H., Sills, R., and Pifer, E., (2012), "Development of 3D Ice Accretion Measurement Method," AIAA-2012-2938, presented at the 4th AIAA Atmospheric and Space Environments Conference, June 25-28.

[5]Kohonen, T., (2001), *Self-Organizing Maps*, Berlin: Springer-Verlag, 3rd ed.

[6]McClain, S., Tino, T., and Kreeger, R., (2011), "Ice Shape Characterization Using Self-Organizing Maps," *Journal of Aircraft*, Vol. 48, No. 2, March-April.

[7]Wright, W.B., 2002, "User Manual for the NASA Glenn Ice Accretion Code LEWICE," NASA/CR-2002-211793.

[8]Croce, G., De Candido, E., Habashi, W. G., Munzar, J., Aubé M. S., Baruzzi, G. S., and Aliaga, C., 2010, "FENSAP-ICE: Analytical Model for Spatial and Temporal Evolution of In-Flight Icing Roughness," Journal of Aircraft, 47(4), pp. 1283-1289.

[9]Tino, P., "Intelligent Data Analysis: Topographic Maps of Vectorial Data," *COMP/06-20233/LM Intelligent Data Analysis*, Course Notes, University of Birmingham, 2006.

[10]Belkin, M. and Niyogi, P., Laplacian Eigenmaps for Dimensionality Reduction and Data Representation," *Neural Computation*, Vol. 15, No.6., pg 1373-1396, 2003.

[11]Bishop, C. M., Svensen, M., and Williams, C. K. I., "The Generative Topographic Mapping," *Neural Computation*, Vol. 10, No. 1, pg 215-234, 1998.

[12]Utsugi, A., "BSOM1: Bayesian Self-Organizing Map Ver. 1.0," 1996.

[13]Alahakoon, D., Halgamuge, S. K. and Sirinivasan, B., (1998), "A Self Growing Cluster Development Approach to Data Mining," Proceedings of IEEE International Conference on Systems, Man and Cybernetics, San Diego, USA, pp 2901-2906.

[14]Jeck, R. K., 2002, "Icing Design Envelopes (14 CFR Parts 25 and 29, Appendix C) Converted to a Distance-Based Format," DOT/FAA/AR-00/30.